Experimental and Modeling Analysis of Detonation in Circular Arcs of the Conventional High Explosive PBX 9501

Mark Short[a,*], Eric K. Anderson[a], Carlos Chiquete[a], Scott I. Jackson[a]

[a]*Los Alamos National Laboratory, Los Alamos, NM 87544, USA*

Abstract

We examine the diffraction dynamics of a two-dimensional (2D) detonation in a circular arc of the conventional HMX-based, high performance, solid explosive PBX 9501, for which the detonation reaction zone length scale is estimated to be of the order of 100-150 μm. In this configuration, a steady propagating detonation will develop, sweeping around the arc with constant angular speed. We report on results from three PBX 9501 arc experiments, exploring the variation in linear speed on the inner and outer arc surfaces for the steady wave, along with the structure of the curved detonation front, as a function of varying inner surface radius and arc thickness. Comparisons of the properties of the motion of the steady wave for each arc configuration are then made with a spatially-distributed PBX 9501 reactive burn model, calibrated to detonation performance properties in a 2D planar slab geometry. We show that geometry-induced curvature of the detonation near the inner arc surface has a significant effect on the detonation motion even for conventional high explosives. We also determine the detonation driving zone structure for each arc case, and thus the subsonic regions of the flow that determine the influence of the arc geometry on the detonation propagation. In addition, streamline paths and reaction progress isolines are calculated. We conclude that a common approximation for modeling conventional high explosive detonation, wherein the shock-normal detonation speed is assumed equal to the Chapman-Jouguet speed, can lead to significant errors in describing the speed at which the detonation propagates.

Keywords:
Detonation, Condensed-phase, Arc geometry, Curvature, Diffraction

*Corresponding author:
Email address: short1@lanl.gov (Mark Short)

1. Introduction

Geometry-induced diffraction of a detonation in a condensed-phase high explosive (HE) affects the detonation propagation dynamics due to the resulting modification of the structure of the finite-length detonation reaction zone. An ideal geometry to examine the primary effects of diffraction is the two-dimensional (2D) circular arc [1–3], shown schematically in Fig. 1. In particular, after relaxing from an initiation transient, a steady detonation sweeping around the arc with constant angular speed will develop in the circular arc configuration. The energy release within the subsonic detonation-driving-zone (or DDZ), i.e. the region bounded by the non-planar detonation shock and sonic flow locus (relative to the frame of the steady rotating shock), controls the propagation properties of the detonation [4]. The circular arc configuration is also important in gaseous explosive systems to the understanding of the diffraction mechanics of detonation propagating in a rotating detonation engine [5–7].

A number of physical insights on the dynamics of a steadily propagating, diffracting detonation in a 2D circular arc of HE have been recently been uncovered in [1, 2]. For example, the authors found that for a fixed inner arc surface radius, beyond a critical arc thickness, the angular speed of the detonation limits to a constant, independent of either further increases in the arc thickness or changes in the type of confinement on the outer arc surface. This is a result of the subsonic DDZ flow region detaching from the outer arc surface, with supersonic flow now surrounding the DDZ. Also, the authors of [1, 2] found that a small radial layer of the arc attached to the inner arc surface played a disproportionate role in controlling the angular speed of the detonation propagation. In this layer, there is a strong influence of both the detonation curvature and the material confinement properties on the inner arc surface.

In addition to the theory-based studies [1, 2], Short et al. [3] describe an experiment in a circular section of the insensitive high explosive (IHE) PBX 9502 (95 wt.% TATB (2,4,6-triamino-1,3,5-trinitrobenzene)/5 wt.% Kel-F 800 poly(chlorotrifluoroethylene-co-vinylidene fluoride)) designed to measure the structure and speed of a 2D steady detonation in a circular arc geometry. The arc section had an inner radius of R_i = 64.98 mm, an outer radius of R_e = 89.97 mm and was 200 mm wide to ensure that the hydrodynamic flow along the centerline of the arc remained two-dimensional during the course of the experiment (Fig. 2). Associated reactive burn modeling showed that the sonic flow locus of the DDZ largely lies at the

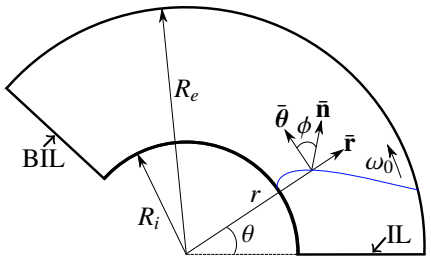

Figure 1: The 2D circular arc geometry and its polar coordinate representation. A schematic detonation shock surface is shown in blue. Here, BIL is the detonation breakout imaging line, while IL is the initiation line.

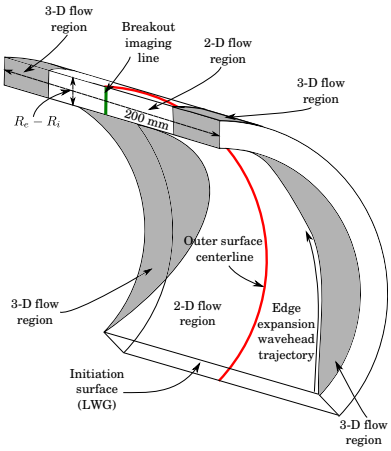

Figure 2: Schematic of the circular arc section explored both in [3] and the current study. A region of 3D flow propagates from the left and right outer edges of the section toward the arc center plane. However, the 200 mm arc section width is such that the flow along the inner and outer surface centerlines remains two-dimensional, where the time-of-arrival and detonation front shape measurements are taken.

end of, or within, the fast reaction stage of the PBX 9502 detonation [3] for the 64.98x89.97 mm arc, with the largest area section of the DDZ lying close to the inner arc surface.

A number of other experiments with either the circular arc section or rib geometry in TATB-based (insensitive) explosive formulations have also been conducted [8–10], although all had arc section widths smaller than both the inner and outer arc circumferential distances. Two-dimensional reactive burn simulations of the arc configurations in [8–10] have been conducted by Tarver and Chidester [11] and Ioannou et al. [12]. To date, the diffraction dynamics of a 2D steady detonation in a circular arc configuration of a conventional high explosive (CHE) have not been examined. Given the extensive use of CHEs in precision munition applications, it is important to demonstrate that we can accurately simulate and understand CHE detonation dynamics in geometries other than simplified 2D planar slabs or 2D axisymmet-

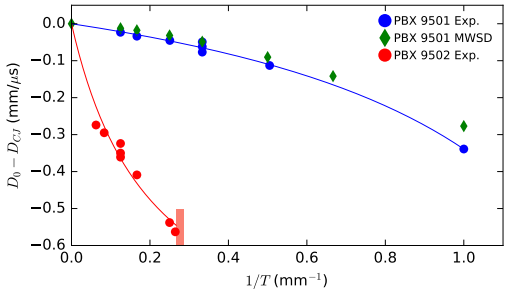

Figure 3: Comparison of the thickness effect variation for PBX 9501 and PBX 9502 [13], showing the axial detonation speed (D_0) relative to the Chapman-Jouguet speed (D_{CJ}) as a function of inverse slab thickness $1/T$. Here D_{CJ} = 8.8 mm/μs for PBX 9501 and D_{CJ} = 7.8 mm/μs for PBX 9502. Also shown are the speeds D_0 obtained in the calibration of the PBX 9501 MWSD reactive burn model (§3).

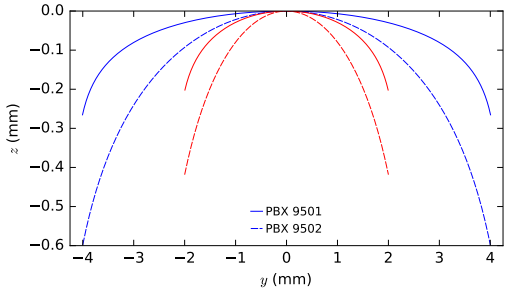

Figure 4: The detonation shock shape variation in PBX 9501 and PBX 9502 slabs of thicknesses 4 mm (red) and 8 mm (blue), showing the shock displacement (z) relative to the charge center ($y = 0, z = 0$) as a function of slab width coordinate (y).

ric cylinders [13]. This is the purpose of the current study.

In the following, we examine the CHE PBX 9501 (95 wt.% HMX explosive crystals bonded with a binder mixture of 2.5 wt.% Estane and a 2.5 wt.% eutectic mixture of bis(2,2-dinitropropyl)acetal and bis(2,2-dinitropropyl)formal (BDNPA/BDNPF)). PBX 9501 has detonation performance properties that are characteristic of most types of CHEs [13]. The total PBX 9501 detonation reaction zone length is on the order of 100-150 μm, compared to the more complex structure of the IHE PBX 9502 detonation, having a fast reaction layer of size $\approx$ 100-150 μm followed by a slower reaction depletion layer of length $\approx$ 1.5 mm [3]. Figure 3 shows a comparison of the experimentally-determined steady axial detonation propagation speeds for PBX 9501 and PBX 9502 in 2D planar geometries (slabs) as a function of $1/T$, where T is the slab thickness [13]. The detonation speeds of PBX 9502 decrease significantly more rapidly with decreasing T than for PBX 9501. Primarily, the flow divergence effects associated with a shock curvature of a given size will more significantly affect the longer reaction zone structure of a PBX 9502 detonation. In particular, the reaction progress along the DDZ sonic flow surface will be smaller than that for a PBX 9501 detonation. The failure thickness for a PBX 9502 detonation is significantly larger than for PBX 9501, in the region $3.5 < T < 3.75$ mm for PBX 9502, and smaller than $T = 0.8$ mm for PBX 9501 [13]. A comparison of the detonation shock shapes for the same slab geometry thicknesses are shown in Fig. 4, revealing some significant features. While the PBX 9501 detonations are flatter in the center of the charges than for the equivalent PBX 9502 detonations, significantly larger shock curvatures exist near the charge edges for PBX 9501. The near-edge curvature variation is significant since, as noted above, a detonation in a circular arc configuration is largely controlled by the shock curvature variation in a layer near the inner arc surface [1–3].

In the current study, three experiments are described examining the variation in speed and shock shape of the steady rotating detonation as a function of varying inner arc surface radius and arc thickness. The arc results are then used to validate a new PBX 9501 reactive burn model, calibrated via the slab geometry detonation properties in Figs. 3 and 4. Physical insights about the effects of the circular arc geometry on the PBX 9501 detonation reaction zone structure and speed are explored through the reactive burn model. This includes an examination of the DDZ structures to determine the subsonic flow region in each of the arcs influencing the detonation propagation.

2. PBX 9501 Circular Arc Section Experiments

Three different PBX 9501 arc section experiments were conducted with dimensions as follows (see Figs. 1-2): for arc 1, 65.35 mm (R_i) x 67.35 mm (R_e) x 200 mm (width); for arc 2, 65.47 mm (R_i) x 69.97 mm (R_e) x 200 mm (width); and for arc 3, 100.35 mm (R_i) x 120.35 mm (R_e) x 200 mm (width). The angular extent of each of the arcs was $\approx 3\pi/4$ radians. The densities of arcs 1 and 3 were 1.841 g/cm^3, while arc 2 was 1.840 g/cm^3. Polycarbonate (PC) supports of 9.2 mm nominal thickness were glued to the inner arc surfaces for stability during machining (Fig. 5). Time-of-arrival (ToA) wire diagnostics were located around the centerline of the outer arc surface (Fig. 2), while ToA shorting pins were inserted through the PC supports along the centerline on the inner surface. The ToA diagnostics are used to measure the linear detonation speed on the inner and outer surface centerlines. Their respective circumferential positions relative to the first pin or wire that triggered on each centerline are shown in Fig. 6. The breakout times of successive sections of the detonation shock as a function of radial coordinate along the centerline of the arc

Table 1: Linear speeds of the steady detonation motion along the inner ($r = R_i$) and outer ($r = R_e$) arc surfaces for the 3 arc tests showing a comparison between experimental (Exp.) measurements and the reactive burn (MWSD) model.

R_i-R_e (mm) Exp.	Speed (R_i) (mm μs^{-1}) Exp.	Speed (R_i) (mm μs^{-1}) MWSD	Speed (R_e) (mm μs^{-1}) Exp.	Speed (R_e) (mm μs^{-1}) MWSD
65.35-67.35	8.582(±0.013)	8.572	8.831(±0.003)	8.834
65.47-69.97	–	8.582	9.186(±0.006)	9.172
100.35-120.35	8.664(±0.021)	8.630	10.411(±0.018)	10.350

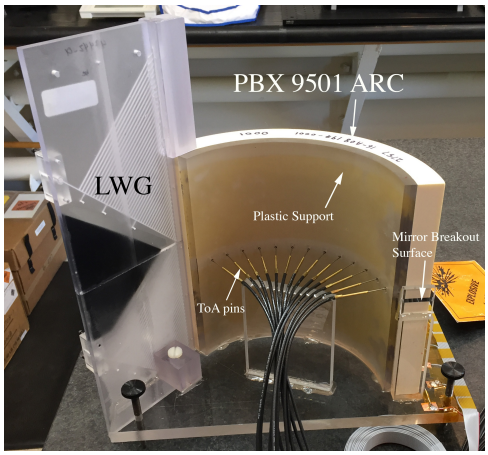

Figure 5: Image of the 100.35x120.35x200 mm PBX 9501 arc test.

end surface was measured by streak camera imaging of the destruction time of an illuminated mirrored surface (see Fig. 1-2 and 5). The outer radius (R_e) dimensions of each arc, listed above, were obtained by fitting a circle through an optical comparator measurement of the Cartesian locations of the ToA wires. Since there was no direct method of measuring the arc inner radius (R_i) due to the PC support, the end-surface detonation breakout time record for each test was used to determine the arc thickness, using a fiducial image to determine the position of the arc edges. The detonation is initiated uniformly along the width of each arc section with a line wave generator (LWG) placed in direct contact with the PBX 9501 arc (Fig. 5). The LWG generator thickness was 3.5 mm.

For each arc test, the relative trigger times for the ToA diagnostics along the inner and outer arc surface centerlines with circumferential distance along each line are shown in Fig. 6. The resulting detonation speeds are determined by a least squares fitting of a linear distance-time function once the detonation has relaxed to a steady rotating propagation mode. Steady-state propagation was determined by calculating where the standard deviation about a local mean in inter-ToA diagnostic speeds, marching backwards from the final ToA record on each surface, exceeded a threshold. The

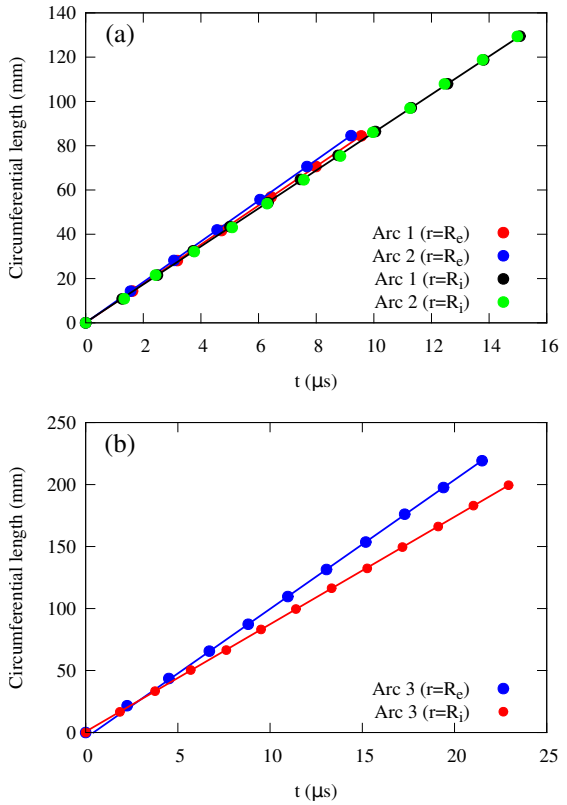

Figure 6: (a) Trigger times (circles) of the ToA diagnostics along the inner ($r = R_i$) and outer ($r = R_e$) arc centerlines as a function of inter pin/wire circumferential distance for arcs 1 (65.35x67.35 mm) and 2 (63.47x69.97 mm), relative to the first triggering of pins/wires on each surface. On the outer surface, wires 1-4 did not register a coherent signal for either arc. The gradient of the solid lines are the linear speeds of the steady detonation shown in table 1. (b) As for (a), but for arc 3 (100.35x120.35 mm).

resulting speeds, with standard deviations, are shown in table 1, and the corresponding distance-time functions shown in Fig. 6. Note that we did not record a meaningful steady speed along the inner surface of arc 2 (65.47x69.97 mm), where inter-pin speed variations were consistently $O(100)$ m/s along the surface. However, the front shape image for the arc 2 test showed the presence of jetting between the inner arc surface and the PC layer, likely caused by an air gap between the

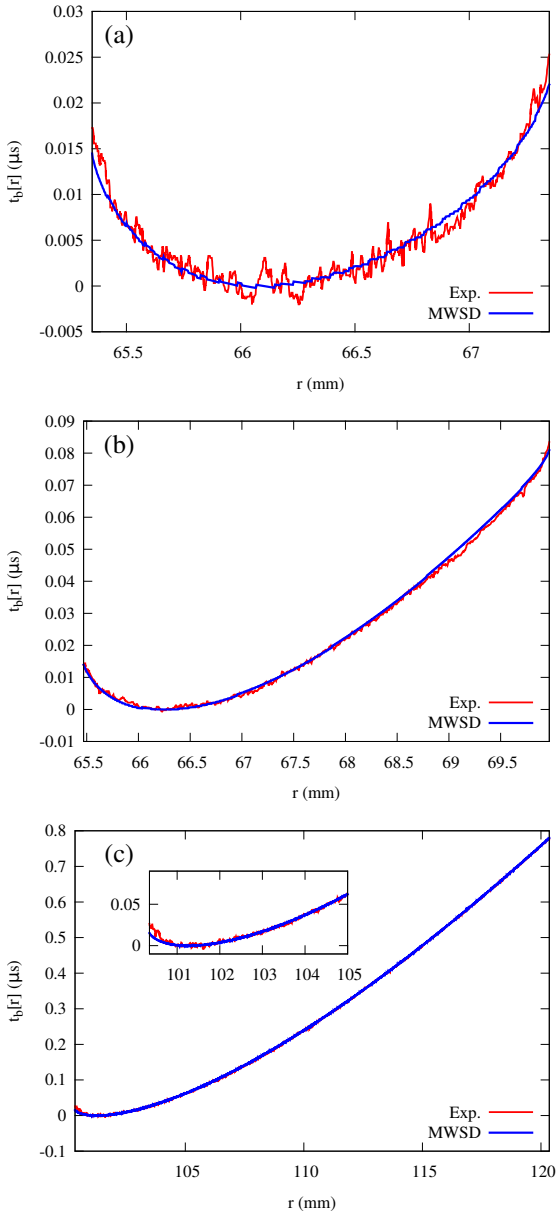

Figure 7: Relative breakout times t_b from the end of the arc surface (Fig. 1-2 and 5) for each point on the detonation shock as a function of radial coordinate for (a) 65.35 mm (R_i) x 67.35 mm (R_e), (b) 65.47 mm (R_i) x 69.97 mm (R_e) and (c) 100.35 mm (R_i) x 120.35 mm (R_e) arcs, comparing experimental results with the reactive burn (MWSD) model predictions.

two surfaces. The jetting likely influenced the pin triggering mechanism. For arc 1, the angular speed ω_0 of the detonation based on the $r = R_i$ data is $\omega_0 = 0.1313$ rad/μs, while $\omega_0 = 0.1311$ rad/μs based on $r = R_e$ data, consistent with a steady wave sweeping around the arc. For arc 2, $\omega_0 = 0.1313$ rad/μs ($r = R_e$). Thus, the detonation rotates around the two arcs with similar R_i but different thicknesses with similar angular speeds, showing that even for a PBX 9501 arc thickness of 2 mm, the outer arc surface dimension no longer influences the angular speed. For arc 3, $\omega_0 = 0.08641$ rad/μs ($r = R_i$) and $\omega_0 = 0.08651$ rad/μs ($r = R_e$), again showing good consistency.

The relative breakout times t_b from the end of the arc surface for each point on the detonation shock as a function of radial location are shown in Fig. 7 for the 3 arc tests. The heterogeneous microstructure of PBX 9501 is reflected in the observed noise levels, particularly for the scale of the arc 1 test. As a result, the first point of breakout, shifted to $t_b(r) = 0$, is obtained from the gradient of the breakout shapes dt_b/dr using a Savitzky-Golay filter. For arc 1, the breakout shape is moderately symmetric across the arc thickness. Arcs 2 and 3 have features similar to those observed for the PBX 9502 arc [3]. The initial point of breakout occurs close to the inner arc surface. There is significant breakout surface curvature in the region of the inner arc, while the outer sections of the breakout surface are more linear.

3. PBX 9501 Reactive Burn Modeling

Reactive burn modeling allows the structure of the detonation driving and reaction zone in the PBX 9501 arc configuration to be explored. Using a newly calibrated reactive burn model for PBX 9501, we now describe computational simulations of detonation in the three circular arcs with inner and outer radii given in §2, with each of the arcs extending the angular region $0 \le \theta \le 3\pi/2$ in polar coordinates (r, θ). The PBX 9501 is surrounded by a low-density elastomer. This is a similar computational similar set-up to that used in [3], but with PBX 9502 replaced by PBX 9501. As in [3], we model the flow in both the arc-geometry explosive and elastomer with the compressible Euler equations,

$$\frac{D\rho}{Dt} + \rho \nabla \cdot \mathbf{u} = 0, \quad \frac{D\mathbf{u}}{Dt} = -\frac{1}{\rho}\nabla p, \quad \frac{De}{Dt} = \frac{p}{\rho^2}\frac{D\rho}{Dt}, \quad (1)$$

for density ρ, pressure p, particle velocity $\mathbf{u} = (u, w)$, specific internal energy e and time t. The material derivative $D/Dt = \partial/\partial t + \mathbf{u} \cdot \nabla$. In the HE, assuming a reactant state burning to a product state, the internal energy e and specific volume $v = 1/\rho$ for the reactant/product mixture is $e = (1 - \lambda)e_R(p_R, v_R) + \lambda e_P(p_P, v_P)$ and $v = (1 - \lambda)v_R + \lambda v_P$, where $\{\}_R$ refers to the state in the reactant material and $\{\}_P$ to the product. Here λ represents the reaction progress variable in the conversion of reactants ($\lambda = 0$) into products ($\lambda = 1$). The reactant and product equations of state (EOS) have the same (Davis) form as in [3], except they are reparameterized here for PBX 9501, with the EOS parameters now taking the values given in tables 2 and 3. To

Table 2: Davis product EOS parameters

a_P	b	n_P	p_c (GPa)	v_c (cm^3/g)	k_P
0.7965	0.8258	1.8679	3.6549	0.8291	1.3000

Table 3: Davis reactant EOS parameters

A (mm/μs)	B	C	Z	Γ_R^0	e_0 (mm^2/μs^2)
2.1987	3.6262	0.3389	0	0.6700	5.8500

close the system, we invoke pressure equilibrium and volume (density) equality as in [3], i.e. $p = p_P = p_R$, and $v = v_P = v_R$.

For PBX 9501, the reaction rate is given by

$$\frac{D\lambda}{Dt} = r, \quad r = kp^n(1-\lambda)^\nu. \tag{2}$$

The rate parameters k, n and ν are calibrated to reproduce the detonation thickness effect and front shape data in a 2D planar slab geometry [13] using the merit-function-based fitting approach in [14], whereby $k = 0.0036010\ \mu s^{-1}GPa^{-n}$, $n = 3.0$ and $\nu = 0.76781$. Figure 3 shows the thickness effect variation obtained as part of the reaction rate parameter calibration process. We term this as a modified Wescott-Stewart-Davis model (MWSD) for PBX 9501. For an initial density $\rho_0 = 1.832$ g/cm^3, $D_{CJ} = 8.80$ mm/μs, while the ZND detonation reaction zone length is $\approx 96\ \mu$m. The elastomer EOS is that used in [3]. For the arc calculations, the flow equations in the HE and elastomer regions are integrated with a cell-centered finite volume method on a Cartesian mesh [4]. Material interfaces are treated with a Ghost Fluid method as described in [15], where a local linearized Riemann solution is used to fill the real fluid states. With adaptive mesh refinement, we find that a mesh spacing of 3.125 μm is needed to ensure mesh converged solutions. The wave is initiated with a hot-spot as in [3] and allowed to relax to the steady rotating propagation mode.

Angular speeds of the steady detonation from the MWSD model computations are determined to be $\omega_0 = 0.13116$ rad/μs for the 65.35x67.35 mm arc, $\omega_0 = 0.13108$ rad/μs for the 65.47x69.97 mm arc and $\omega_0 = 0.08600$ rad/μs for the 100.35x120.35 mm arc. The MWSD model based calculation of ω_0 can then be used to generate the linear speeds $\omega_0 R_i$ and $\omega_0 R_e$ on $r = R_i$ and $r = R_e$, respectively, shown in table 1. The agreement with the experiments is good, showing that the MWSD model is capturing the salient physical mechanisms of the detonation propagation. For the MWSD model of the 65.35x67.35 mm and 65.47x69.97 mm PBX 9501 arcs, the linear speeds on $r = R_i$ are almost equal, showing that even for a 2 mm thick arc with a fixed inner radius of ≈ 65 mm, the detonation angular speed no longer depends on the arc thickness. For each arc, the linear speeds on $r = R_i$ depart significantly from $D_{CJ} = 8.8$ mm/μs, by 228 m/s for the 65.35x67.35 mm arc and 170 m/s for the 100.35x120.35 mm arc. Curvature effects, particularly near the inner surface as we demonstrate below, have a significant influence on the propagation even for the CHE PBX 9501. Figure 7 also shows a comparison between the relative detonation shock breakout times from the MWSD modeling and the experiment for each arc geometry. In all cases, the agreement is excellent, further validating the MWSD PBX 9501 model across a range of arc sizes.

Figure 8 shows the detonation driving zone structure in steady flow for each arc simulation. The subsonic DDZ flow is bounded by the detonation shock and sonic flow loci [2]. Sonic flow is measured relative to a frame rotating with the detonation shock front, along which each location on the shock moves with speed $(r\omega_0 \sin\theta, -r\omega_0 \cos\theta)$, and is determined by the locus of points for which $M = [(u + r\omega_0 \sin\theta)^2 + (w - r\omega_0 \cos\theta)^2)]^{1/2}/c_{HE} = 1$, where c_{HE} is the frozen sound speed [2]. Also shown in Fig. 8 are a series of steady flow streamlines, representing the spatial paths obtained from the integration of $dx/dy = (u + r\omega_0 \sin\theta)/(w - r\omega_0 \cos\theta)$, along with HE/elastomer material interface locations and a series of reaction progress isolines for $\lambda = 0.5$, 0.9 and 0.99. Figure 9 shows the normal surface speed D_n and curvature κ variations along the detonation shock front for each arc, obtained by interpolating a smooth function through the shock shapes and using geometric constraints [1] to obtain D_n and κ.

Figure 8a shows the DDZ for the 65.35x67.35 mm arc. The DDZ has a broadly curved, crescent like, appearance, with the shock front oblique to the incoming flow except in the central regions. The DDZ is spatially thin for PBX 9501 detonation, $\approx 80\ \mu$m wide in the central part of the arc. Significant D_n and κ variations are observed in a layer within ≈ 0.5 mm of $r = R_i$ (Fig. 9), associated with limited reaction (Fig. 8a, 10). The shock curvature is smaller in the central part of the arc, where reaction progress is greater, before increasing again at the outer section of the arc. Flow streamlines enter the DDZ in a circular fashion, and are deflected both by the shock front and the onset of reaction. However, on the scale of the DDZ (Fig. 8a), the deflections are small.

The DDZ structure for the 65.47 mm x 69.97 mm arc is shown in Fig. 8b. The detonation rotates at a very similar angular speed, $\omega_0 = 0.13108$ rad/μs, to the 65.35x67.35 mm arc, for which $\omega_0 = 0.13116$ rad/μs. Near $r = R_i$, we again observe a crescent-like structure

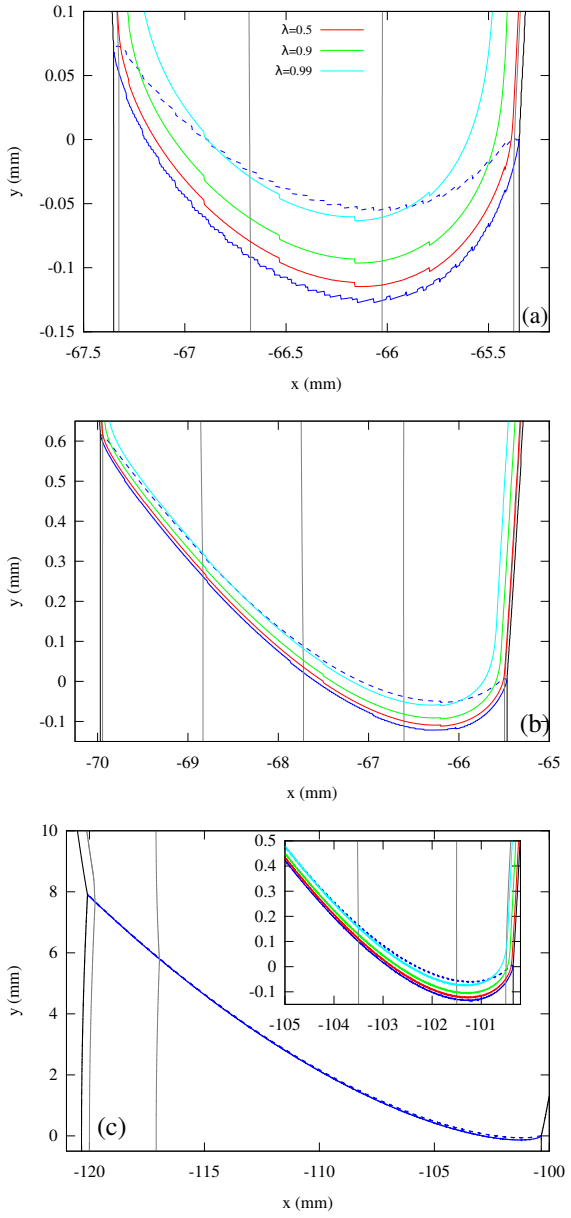

Figure 8: The structure of the subsonic DDZ region in (a) the 65.35x67.35 mm arc, (b) the 65.47x69.97 mm arc and (c) the 100.35x120.35 mm arc. In each case, the solid blue line is the shock front locus, while the dashed blue line is the corresponding sonic flow locus. The gray lines are steady flow streamlines and the black lines are material interfaces. Reaction progress contours are also shown for $\lambda = 0.5$, 0.9 and 0.99. All plots are shown in Cartesian coordinates, and centered such that the detonation shock on $r = R_i$ lies at $(-R_i, 0)$.

to the DDZ, containing a boundary layer at $r = R_i$ of size ≈ 0.5 mm where D_n and κ variations are significant (Fig. 9), and also very similar spatially to those observed for the 65.35x67.35 mm arc. Outside of this inner layer, we encounter a quasi-1D detonation structure, in which curvature variations are small (Fig 9b),

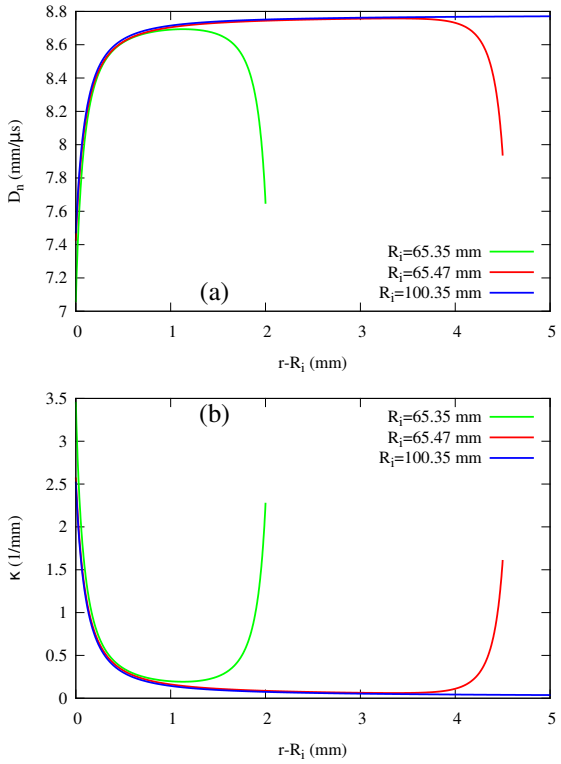

Figure 9: Variation of (a) the normal speed D_n and (b) the curvature κ along the detonation shock surface as a function of radial coordinate r relative to $r = R_i$ for the 3 arc geometries. For the 100.35x120.35 mm arc, only the region $0 \le r - R_i \le 5$ mm is shown.

reactant is almost depleted along the sonic flow line (Fig. 10), and the normal speed D_n is close to D_{CJ} (=8.8 mm/μs) [Fig 9a]. The shock front in this outer section is oblique to the incoming circular flow, allowing it to rotate at speed $\omega_0 = 0.13108$ rad/μs, with its motion controlled by the inner layer DDZ structure, consistent with the asymptotic theory developed in [1]. Figure 11 shows an overlay of the DDZ structures for the 65.35x67.35 and 65.47x69.97 mm arcs. For a layer of size ≈ 1 mm attached to $r = R_i$, the structures closely overlap. Given the similarity in the angular speeds, we conclude that the energy release in the quasi-1D section of the arc does not contribute to the propagation dynamics. Near $r = R_e$, the sonic layer moves internal to the reaction zone due to the presence of the Prandtl-Meyer fan on the outer boundary, meeting the detonation shock at $r = R_e$.

The DDZ structure for the larger 100.35x120.35 mm arc is shown in Fig. 8c. The overall properties are similar to those of the 65.47x69.97 mm arc, with the bulk of the oblique detonation outside of the inner layer being sweep around the arc by the controlling inner layer DDZ structure. Flow streamline deflections are more noticeable on the scale of Fig. 8c. Significant D_n and κ

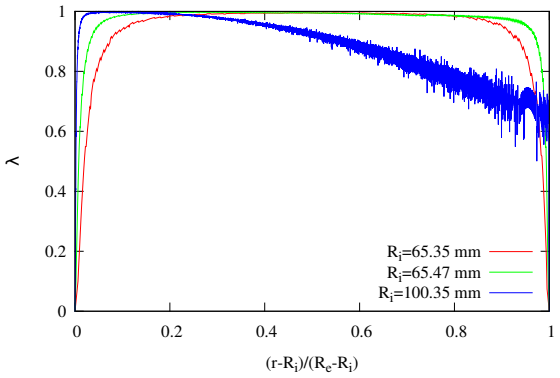

Figure 10: Reaction progress λ along the sonic flow locus for each arc as a function of scaled radial coordinate $(r - R_i)/(R_e - R_i)$.

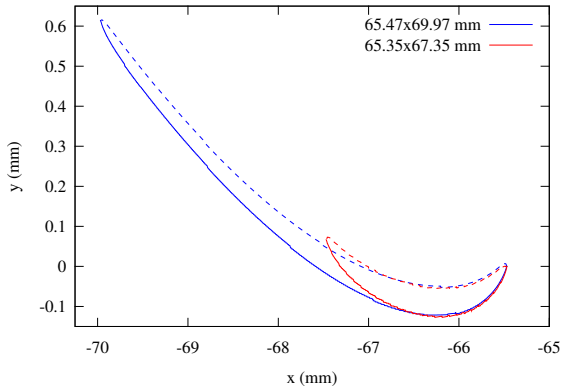

Figure 11: Comparison of the DDZ structures between the 65.35x67.35 and 65.47x69.97 mm arcs. The DDZ structure for the 65.35x67.35 mm arc has been shifted to the left by 0.12 mm so that the detonation shock points on the inner arc surfaces are coincident.

variations are again present in the inner layer, even for the larger R_i. In the outer layer, the sonic locus is drawn into the reaction zone at a comparatively earlier stage relative to $R_e - R_i$ than the 65.47x69.97 arc (Fig. 10), due to the oblique flow.

4. Summary

We have described three experiments on 2D steady detonation of the high performance, HMX-based conventional high explosive (CHE) PBX 9501 in a circular arc geometry, measuring linear propagation speeds on the inner and outer arc surfaces, along with the detonation shock front shape. We have used this data to validate a MWSD reactive burn model, previously calibrated to 2D planar slab geometry data, demonstrating very good agreement. Using the MWSD model, an extensive study of the detonation driving structure (shock and sonic flow loci) for the three arcs was undertaken, including analysis of flow streamlines and reaction progress contours. This analysis shows that for PBX 9501, curvature variations in a layer near the inner arc surface, $r = R_i$, largely controls the propagation dynamics. We conclude that geometry-induced curvature effects have a significant influence on the detonation structure and dynamics even for CHEs, yielding speeds on the inner arc surface that can be significantly below D_{CJ}. Hence, for complex geometries such as the arc, assuming that the detonation runs at the Chapman-Jouguet speed can lead to significant errors for modeling detonation performance of CHEs.

References

References

[1] M. Short, J. Quirk, C. Meyer, C. Chiquete, Steady detonation propagation in a circular arc: a Detonation Shock Dynamics model, J. Fluid Mech. 807 (2016) 87–134.

[2] M. Short, J. Quirk, C. Chiquete, C. Meyer, Detonation propagation in a circular arc: reactive burn modelling, J. Fluid Mech. 835 (2018) 970–998.

[3] M. Short, C. Chiquete, J. Bdzil, J. Quirk, Detonation diffraction in a circular arc geometry of the insensitive high explosive PBX 9502, Combust. Flame 196 (2018) 129–143.

[4] M. Short, J. Quirk, High explosive detonation-confiner interactions, Annu. Rev. Fluid Mech. 50 (2018) 215–242.

[5] H. Nakayama, J. Kasahara, A. Matsuo, I. Funaki, Front shock behavior of stable curved detonation waves in rectangular-cross-section curved channels, Proc. Combust. Instit. 34 (2013) 1939–1947.

[6] M. Short, C. Chiquete, J. Quirk, Propagation of a stable gaseous detonation in a circular arc configuration, Proc. Combust. Instit. 37 (2019) 3593–3600.

[7] V. Rodriguez, C. Jourdain, P. Vidal, R. Zitoun, An experimental evidence of steadily-rotating overdriven detonation, Combust. Flame 202 (2019) 132–142.

[8] S. Lubyatinsky, S. Batalov, A. Y. Garmashev, V. Israelyan, O. Kostitsyn, B. Loboiko, V. Pashentsev, V. Sibilev, E. Smirnov, V. Filin, Detonation propagation in 180° ribs of an insensitive high explosive, in: Shock Compression of Condensed Matter, CP 706, American Institute of Physics, 2003, pp. 859–862.

[9] T. Zhao, Q. Li, F. Zhao, C. Sun, L. Han, Z. He, W. Gao, An experimental study of detonation propagation in the arc insentitive high explosive initiated on the basal plane, in: Eleventh International Detonation Symposium, Office of Naval Research, ONR 333000-5, 1998, pp. 1023–1028.

[10] P. Souers, S. Anderson, B. Hayes, J. Lyle, E. Lee, S. McGuire, C. Tarver, Corner turning rib tests on LX-17, Propell. Expl. Pyrotechn. 23 (1998) 200–207.

[11] C. Tarver, S. Chidester, Ignition and growth modeling of detonating TATB cones and arcs, in: Shock Compression of Condensed Matter, CP 955, American Institute of Physics, 2007, pp. 429–432.

[12] E. Ioannou, S. Schoch, N. Nikiforakis, L. Michael, Detonation propagation in annular arcs of condensed phase explosives, Phys. Fluids 29 (2017) 116102.

[13] S. Jackson, M. Short, Scaling of detonation velocity in cylinder and slab geometries for ideal, insensitive and non-ideal explosives, J. Fluid Mech. 773 (2015) 224–266.

[14] C. Chiquete, M. Short, C. Meyer, J. Quirk, Calibration of the Pseudo-Reaction-Zone model for detonation wave propagation, Combust. Theory Modell. 22 (2018) 744–776.

[15] J. Quirk, Towards an analysis of the Ghost Fluid method, Technical Report LA-UR-19-30913, Los Alamos National Laboratory, Los Alamos, NM., 2006.